The Influence of UiO-66 Metal–Organic Framework Structural Defects on Adsorption and Separation of Hexane Isomers

Sławek, Andrzej; Jajko, Gabriela; Ogorzały, Karolina; Dubbeldam, David; Vlugt, Thijs J.H.; Makowski, Wacław

DOI
10.1002/chem.202200030

Publication date
2022

Document Version
Final published version

Published in
Chemistry - A European Journal

Chemistry–A European Journal
Research Article
doi.org/10.1002/chem.202200030
Chemistry Europe
European Chemical Societies Publishing
www.chemeurj.org

The Influence of UiO-66 Metal–Organic Framework Structural Defects on Adsorption and Separation of Hexane Isomers

Andrzej Sławek,*[a] Gabriela Jajko,[b] Karolina Ogorzały,[b] David Dubbeldam,[c] Thijs J. H. Vlugt,[d] and Wacław Makowski[b]

Abstract: In this work, adsorption properties of the UiO-66 metal–organic framework were investigated, with particular emphasis on the influence of structural defects. A series of UiO-66 samples were synthesized and characterized using a wide range of experimental techniques. Type I adsorption isotherms for low-temperature adsorption of N_2 and Ar showed that micropore volume and specific surface area significantly increase with the number of defects. Adsorption of hexane isomers in UiO-66 was studied by means of quasi-equilibrated temperature-programmed desorption and adsorption (QE-TPDA) experimental and Monte Carlo simulation techniques. QE-TPDA profiles revealed that only defect-free UiO-66 exhibits distinct two adsorption states. This technique also yielded high-quality adsorption isobars that were successfully recreated using Grand-Canonical Monte Carlo molecular simulations, which, however, required refinement of the existing force fields. The calculations demonstrated the detailed mechanism of adsorption and separation of hexane isomers in the UiO-66 structure. The preferred tetrahedral cages provide suitable voids for bulky molecules, which is the reason for unusual "reverse" selectivity of UiO-66 towards di-branched alkanes. Interconnection of the tetrahedral cavities due to missing organic linkers greatly reduces the selectivity of the defected material.

Introduction

Metal–organic frameworks (MOFs) are a relatively new, but already extensive group of porous materials consisting of metal ions or clusters connected by multidentate organic bridging ligands. Due to their high porosity, rich chemical composition and unique gas adsorption capability, they are of interest for potential clean energy applications, such as gas capture, storage and separation.[1–6] Recently, one of the MOF families that is based on zirconium metal clusters (Zr-MOFs) has attracted a lot of attention. The most well-known representative of this group is $\{Zr_6O_4(OH)_4(BDC)_6\}_\infty$, better known as UiO-66 (University of Oslo material 66).[7] Its secondary building unit (SBU) is formed by hexanuclear zirconium clusters connected by 1,4-benzenedicarboxylate (BDC) ligands that crystallizes in a 12-connected framework with face centered cubic (fcu) topology. Due to such high connectivity of this SBU, the integrity of the structure can be well maintained after removing part of linkers or even clusters. It is worth noting that this kind of Zr-based building blocks are part of more than 25 other structures of this topology showing the reticular chemistry of these Zr-MOFs.[8]

The microporous structure of UiO-66 comprises of octahedral (≈11 Å) and tetrahedral (≈8 Å) cavities connected via triangular-shaped windows (≈7 Å), which is shown in Figure 1. According to many literature reports, UiO-66 exhibits extraordi-

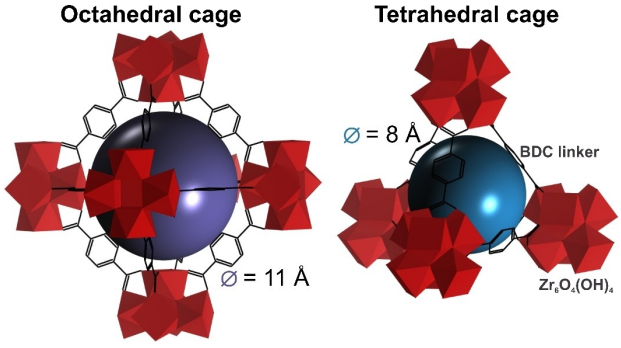

Figure 1. Octahedral (left) and tetrahedral (right) cavities of UiO-66 MOF are marked with color spheres. Zirconium polyhedrals are marked in dark red, while 1,4-BDC linkers in black.

[a] *Dr. A. Sławek*
Academic Centre for Materials and Nanotechnology
AGH University of Science and Technology
Kawiory 30, 30-055 Kraków (Poland)
E-mail: aslawek@agh.edu.pl
[b] *G. Jajko, K. Ogorzały, Prof. Dr. W. Makowski*
Faculty of Chemistry
Jagiellonian University
Ul. Gronostajowa 2, 30-387 Kraków (Poland)
[c] *Dr. D. Dubbeldam*
Van't Hoff Institute for Molecular Sciences (HIMS)
University of Amsterdam
PO Box 94157 1090 GD Amsterdam (The Netherlands)
[d] *Prof. Dr. T. J. H. Vlugt*
Process & Energy Department
Faculty of Mechanical, Maritime and Materials Engineering
Delft University of Science and Technology
Leeghwaterstraat 39, 2628CB Delft (The Netherlands)

Supporting information for this article is available on the WWW under https://doi.org/10.1002/chem.202200030

nary stability being resistant to severe solvents and extremely high temperatures, even up to 500 °C. Moreover, it is also characterized by excellent stress resistance resulting in very high mechanical stability.[9–13]

This material is distinguished by wide functional possibilities. Depending on the synthesis conditions exploited, the BDC linker can be replaced by another substituted linker, which opens up a range of new applications.[14–21] Moreover, the structure of UiO-66 can be modified by introducing framework defects using a modulated synthesis method allowing some of the linkers to be removed and replaced with terminal hydroxyl groups.[6,22,23] A recent review of Feng et al.[24] covers a number of issues related to tailoring defects in UiO-66 including their preparations, characterizations, and potential applications. Linker defect sites have been directly identified experimentally to be occupied by water and hydroxide anions.[25] Increased hydrophilicity of this originally hydrophobic MOF opens a new range of application possibilities, for example in water harvesting,[26] removal of organic water contaminants,[27,28] carbon dioxide capture[29] or catalysis.[30] In recent work, Iacomi et al.[31] showed that the selectivity of other Zr-based MOF-801 in the separation of C3 hydrocarbons may be controlled by its defect chemistry. Structural defects in MOF materials may have a significant impact on their adsorption properties and should be taken into account during the design process.

Metal–organic frameworks are extensively investigated for various separations processes.[3,5] The separation of different alkanes, mainly C5 (pentane) and C6 (hexane) isomers, is an important process in the petrochemical industry. Linear and mono-branched paraffins have low octane numbers (e.g. 24.8 for n-hexane, 73.4 for 2-methylpentane) and need to be removed from the system or undergo further reactions, such as catalytic isomerization.[32] On the other hand, di-branched alkanes are the preferred components of high-octane gasoline (101.7 for 2,3-dimethylbutane).[33–36] Isolation of linear alkanes from the other isomers can be easily performed exploiting the differences in the kinetic diameters of these molecules, for example Ca-LTA zeolite is selective only toward n-alkanes. But yet, selective adsorption of di-branched alkanes is more difficult. It can be achieved through physisorption in nanoporous materials such as zeolites, zeolitic imidazolate frameworks (ZIFs) or metal–organic frameworks (MOFs). Recently, the remarkable performance of the UiO-66 material in sieving mono- and di-branched alkanes has been reported.[37,38] It has been shown that UiO-66 exhibits reverse shape selectivity, i.e. it tends to adsorb multi-branched molecules than more linear ones, which is opposite to that observed for typical adsorbents like zeolites.[39–41] This phenomenon was explained by exploiting differences in pore sizes and diffusion limitations. Experimental work of Mendes et al.[42] confirmed the reverse shape selectivity for the functionalized UiO-66-Br and -NO_2 similar to the parent material. However, at specific conditions, UiO-66-NH_2 exhibited a "normal" sorption hierarchy, i.e. towards less branched molecules, which was not explained. In a recent work of Dong et al.,[43] DFT calculations revealed that -NH_2 and -OH electron-donating groups increase the strength of the interactions between host structure and guest molecules of alkanes. Consequently, they report that UiO-66-NH_2 and UiO-66-OH may be used as potential high-efficiency adsorption and separation adsorbents with the preference for double-branched alkanes. It was also noted that the introduction of bulky -Br, -NO_2 or -NH_2 groups to the BDC linkers of UiO-66 increases the steric hindrance this MOF and reduces its adsorption capacity. In more recent work, Duerinck et al.[44] investigated adsorption of numerous saturated, unsaturated, linear, branched and cyclic hydrocarbons in UiO-66 and its functionalized analogues. A strong influence of the size of cavities on heat of adsorption and selectivity for the molecules of different bulk was reported.

The adsorption properties of microporous materials are usually investigated in the isothermal approach. In this work we also exploit quasi-equilibrated temperature programmed desorption and adsorption (QE-TPDA), a technique different from standard methods because adsorption-desorption equilibrium is controlled by changing the temperature of the sample in contact with the adsorptive at a given partial pressure. This method was successfully exploited for several MOFs, including well-known MOF-5 and ZIF-8.[45–50]

Monte Carlo (MC) methods are well suited for modelling the equilibrium processes.[51] They are based on statistical thermodynamics, where the probability of finding the configuration of a system at equilibrium is determined by the Boltzmann distribution. Unlike molecular dynamics, MC simulations do not follow the physical path of reaching equilibrium, which allows avoiding diffusion limitations and significantly fastens the calculations. In other words, in a single MC simulation, one can only obtain information about the final adsorbent-adsorbate state. Using MC in the Grand Canonical ensemble (GCMC), where the chemical potential μ, volume V and temperature T (μVT) are fixed, it is possible to determine the average number of guest molecules in the pores of the material and their positions. Additionally, one can easily determine thermodynamically important properties, for example heat of adsorption. In general, Monte Carlo simulation provides insight into the adsorption mechanism, allowing a deeper understanding of the experimental results.

In this work, we combined experimental and computational methods to achieve the most comprehensive characteristics of UiO-66 material capacity to adsorb and separate linear and branched hexane isomers. We also put emphasis on how the presence of structural defects influences the adsorption and selectivity of UiO-66 MOF.

Molecular Simulations

We used the TraPPE force field of Martin and Siepmann for adsorbates.[52,53] This is a simplified model of molecules that unites alkyl groups (CH_3, CH_2, CH) into singular interaction centers (pseudoatoms) with effective potentials. This approach considerably reduces the calculation time but also greatly facilitates the development of force fields for interactions between guest molecules and host framework atoms.

We used ideal and defected models of the UiO-66 structure, which remained rigid during the calculations. Although the

rotation of the BDC linkers could have some effect on adsorption equilibrium, in fact, they should wiggle around the equilibrium position. UiO-66_0 stands for the defect-free structure (Figure 2), while UiO-66_32 for the ideal structure, where four 1,4-BDC linkers were removed (32 in 2×2×2 supercell) and replaced by terminal –OH groups. Characteristics of the model structures may be found in Table 1. Crystallography information files were taken from the literature.[26]

Guest-host interactions were calculated using Lennard-Jones (L–J) potential. Due to the fact that the alkane molecules are non-polar (negligible dipole moment), electrostatic interactions have been omitted. The L–J parameters were mixed using standard Lorentz-Berthelot combining rules. The mixed potentials were shifted and truncated to the cutoff distance of 12 Å. As initial parameters for the force field refinement, L–J parameters were taken from DREIDING[54] force field for all framework atoms except those for Zr, which were taken from the UFF force field.[55] Simulation boxes were chosen to be twice larger than unit cells in every direction (2×2×2). Adsorption isobars were calculated using Monte Carlo simulations in the Grand Canonical ensemble (GCMC), with the chemical potential, volume and temperature fixed (μVT). In the simulations we have used 10^4 initialization cycles and $5 \cdot 10^4$ production cycles with equal probabilities of translation, rotation, swap and reinsertion trial moves. Identity change moves were also introduced for the calculations of multicomponent adsorption. In general, GCMC calculations were carried out over a sufficient time to establish an insertion-deletion equilibrium. For calculations of Henry constants and low-coverage enthalpy of adsorption, we used Widom particle-insertion method. All simulations were performed using RASPA 2.0 simulation code.[56,57] Whole set of force field parameters is available in the Supporting Information.

For the quantitative analysis of the average occupation profiles, we distinguished adsorption sites in the porous structure of UiO-66 represented by spheres and/or cylinders. Then, pseudoatoms within a defined adsorption site were counted as adsorbed in a given part of the structure. More detailed information is available in the Supporting Information (Table S4).

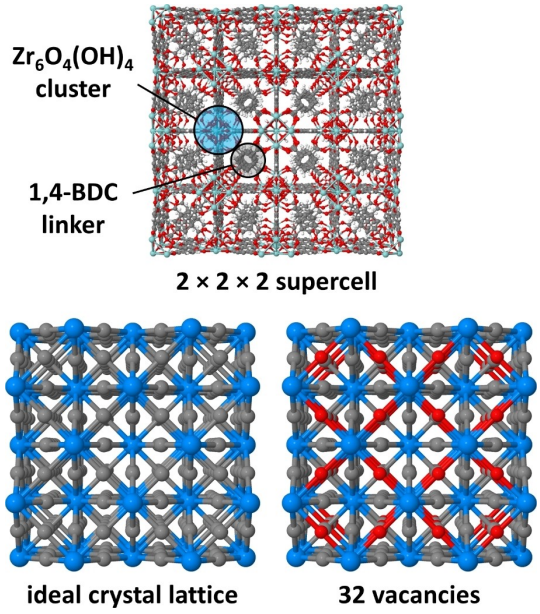

Figure 2. Top: UiO-66 supercell used in this work comprised of 2×2×2 unit cells. Bottom: crystal lattice of UiO-66 is presented here in a simplified form as blue nodes connected via grey linkers. Vacancies in the defected structure are marked in red.

Table 1. Characteristics of the structures used in this work.

	UiO-66_0	UiO-66_32
number of defects	0	32
unit cell formula	$Zr_{24}C_{192}H_{112}O_{128}$	$Zr_{24}C_{160}H_{112}O_{128}$
cell lengths, a = b = c	20.7004 Å	20.7004 Å
cell angles, α = β = γ	90°	90°
simulation box size	2×2×2	2×2×2
framework density[a]	1246	1174
helium void fraction[b]	0.507	0.540
pore volume[c]	0.407	0.460

[a] in kg m^{-3}. [b] unitless. [c] in cm^3 g^{-1}.

Results and Discussion

Basic psysicochemical characterization

The synthesis of the UiO-66 material with different amounts of structural defects – i.e. missing BDC linkers – is well described in the literature.[6,22,58] We used materials synthesized in our previous work,[26] which were a series of three UiO-66 preparations with 2:1 BDC:Zr molar ratio, obtained by heating the reagents at solvothermal conditions (in a sealed autoclave) at 220 °C, 160 °C or 100 °C. Preparations were labelled after temperature of synthesis: UiO-66_220 C, UiO-66_160 C, UiO-66_100 C. Since this type of modulated synthesis yields materials with different amounts of missing BDC ligands, we performed in-depth physicochemical characteristics aimed at studying such defects.

SEM images (Figure S1) showed fine crystalline of the obtained materials with the estimated crystal size of ca. 0.5–0.6 μm for UiO-66_220 C, 0.3 μm for UiO-66_160 C, and 0.1 μm for UiO-66_100 C. Crystals are irregular and tend to aggregate. Crystal structures were already confirmed by the analysis of the powder XRD patterns (Figure S2),[26] which revealed that all materials exhibit very similar reflections that match those modelled for an ideal structure (UiO-66_0). However, for UiO-66_100 C one can observe symmetry-forbidden low-angle reflections at 2Θ of ca. 4 and 6° indicating the presence of defects.[59] FTIR spectra also confirmed the presence of defects in UiO-66_100 C (Figure S3). For UiO-66_100 C, a much more intense band between 2750 and 3750 cm^{-1} was recorded, which is derived from the vibrations of hydrogen-bonded physisorbed MeOH. Additional defect-derived -OH groups result in a larger amount of solvent, which is another indication of the presence of numerous defects in this preparation.[22]

Gas adsorption

Linker vacancies also have a significant impact on the porosity of MOFs.[6] We investigated this phenomenon by measuring adsorption isotherms of nitrogen and argon (Figure S4) – relatively small probe molecules that efficiently fill the micropores. The experiments were conducted at the temperature of liquid nitrogen (77 K) and liquid argon (87 K), respectively, so the saturation vapor pressure p^0 is 1 bar. Type I adsorption isotherms, with no hysteresis loops, were obtained for all studied materials, which is characteristic for microporous materials. At low pressures, adsorption for UiO-66_220 C and UiO-66_160 C is similar and much higher than for UiO-66_100 C. On the other hand, uptake is the highest for UiO-66_100 C at partial pressure close to the saturation conditions ($p/p^0 > 10^{-2}$).

Adsorption measurements of Ar at 87 K provide very accurate data on low-pressure adsorption (p/p^0 of even 10^{-7}), which allows for a detailed analysis of the material microporosity. We calculated the pore size distribution of the studied UiO-66 preparations based on NLDFT analysis of Ar sorption measurements (Figure 3). It is worth noting, that due to the lack of models suitable for MOF materials, we used the one for zeolite/silica. Yet, it fits very well the experimental data (Figure S5). Figure 3 shows that all the studied UiO-66 preparations have micropores of mainly 7 Å and 9.4 Å that correspond to the two types of cavities (Figure 1), which is consistent with the literature reports.[60] Only UiO-66_100 C possess a significant amount of larger pores of 15.5-18 Å that correspond to the voids formed by adjacent cavities. Overall, the physicochemical characteristics clearly show that the number of defects increases in the series UiO-66_220 C, UiO-66_160 C, UiO-66_100 C.

Adsorption isotherms were also used to calculate the pore volume and the specific surface of the materials, using the t-plot and Brunauer-Emmett-Teller (BET) methods, respectively. As presented in Table 2, voids created by the missing linkers significantly increase the micropore volume and specific surface area of the materials. For comparison, we determined pore volumes for n-hexane (nC6) adsorption that is based on liquid adsorbate. This was calculated by the integration of the QE-TPDA profiles (Figure S6). Interestingly, for all materials, the values are ca. 10% higher for N_2 than for nC6, which clearly results from better packing of smaller molecules in the micropores.

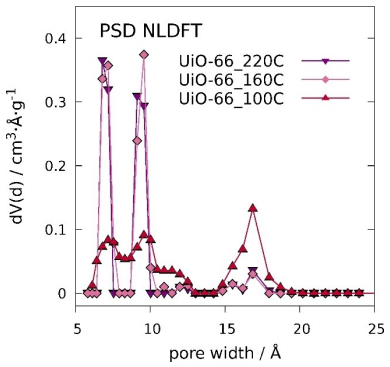

Figure 3. Pore size distribution of UiO-66 preparations under this study determined from Ar adsorption isotherms (NLDFT) at 87 K (Figure S4b).

Table 2. Textural properties of UiO-66 materials under this study obtained from N_2 and Ar adsorption as well as QE-TPDA measurements for n-hexane.

	UiO-66_220 C	UiO-66_160 C	UiO-66_100 C
V_{micro} (nC6)[a]	0.239	0.271	0.329
V_{micro} (N_2)[a]	0.264	0.304	0.361
S_{BET} (N_2)[b]	1141	1271	1447
S_{BET} (Ar)[b]	1099	1198	1297

[a] micropore volume in $cm^3\,g^{-1}$. [b] BET specific surface area in $m^2\,g^{-1}$.

QE-TPDA desorption-adsorption profiles

As shown, defects in UiO-66 influence the adsorption of small probe molecules (Ar, N_2) that effectively fill the micropores. Figure 4 shows experimental quasi-equilibrated thermodesorption and adsorption (QE-TPDA) profiles of hexane isomers in the studied UiO-66 materials. Each profile consists of desorption maxima and adsorption minima, which intensities (relative to

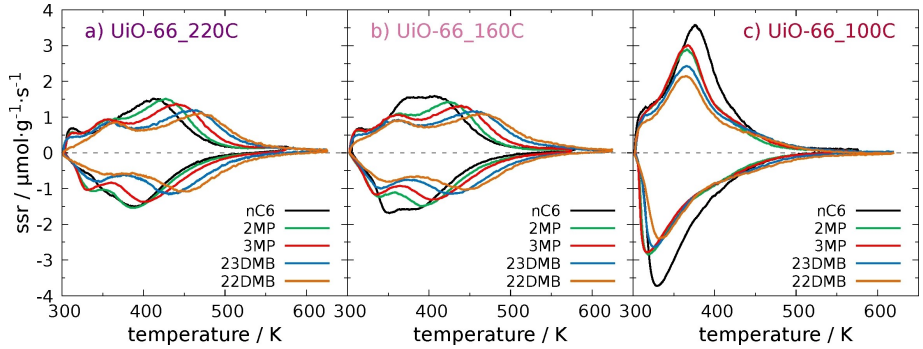

Figure 4. QE-TPDA profiles of hexane isomers on UiO-66 preparations under this study. The partial pressures of n-hexane (nC6), 2-methylpentane (2MP), 3-methylpentane (3MP), 2,3-dimethylbutane (23DMB), and 2,2-dimethylbutane (22DMB) for materials UiO-66_220 C/160 C/100 C are 910/890/780 Pa, 580/690/560 Pa, 510/620/520 Pa, 710/760/660 Pa, 970/1060/830 Pa, respectively ($0.02 < p/p0 < 0.04$).

the baseline) are proportional to the instantaneous amounts of adsorptive that desorb from or adsorb in the material at a particular temperature. Results presented for UiO-66_220 C and UiO-66_160 C are very similar, slight differences are noticeable only for adsorption of nC6. For all adsorbates, two desorption maxima and adsorption minima can be distinguished. Higher-temperature peaks (375–550 K) most likely derive from adsorption in smaller, tetrahedral cavities, while lower-temperature ones (< 375 K) in larger, octahedral ones (Figure 1). Because the UiO-66 framework comprises twice as many tetrahedral than octahedral cavities, high-temperature parts of the profiles have much greater intensity than the low- temperature ones. For both UiO-66_220 C and UiO-66_160 C the temperature of desorption/adsorption increases in series nC6, 2MP, 3MP, 23DMB, 22DMB. This may indicate that the heat of adsorption also increases in the same order, which confirms reverse shape selectivity for alkanes of this MOF.[37] In the case of the most defected UiO-66_100 C, QE-TPDA profiles are more intensive than for other preparations meaning higher adsorption. But more importantly, peaks for all isomers are present at a similar temperature, ca. 350–400 K for desorption and 310–350 K for adsorption, which is lower than for UiO-66_220 C and UiO-66_160 C. This can be caused by lower heat of adsorption, which is expected for larger voids related to the missing linkers. One can also observe a higher-temperature tail at 400–550 K that, most likely, originates from adsorption in intact tetrahedral cavities. The QE-TPDA results clearly show that the structural defects have an impact on the adsorption of alkanes in UiO-66, most likely decreasing the specificity of this MOF towards different isomers. It is worth noting that, based on raw, time-resolved QE-TPDA data, for all experiments adsorbent-adsorbate equilibrium was established almost immediately upon temperature change, which indicates very low diffusion limitations for these systems. Proper integration of the QE-TPDA profiles also results in obtaining more quantitative adsorption isobars,[61,62] that are discussed in the following section.

Force field refinement

To investigate the process of adsorption of alkanes in UiO-66 MOF, one can use Grand Canonical Monte Carlo (GCMC) molecular simulations. These results should be confronted with the experimental data to ensure that the calculations are reliable and indeed reflect the actual physical phenomena. GCMC simulations give information on the average number of molecules adsorbed at the given temperature and pressure at equilibrium conditions. A series of such data are directly comparable with the measured adsorption isotherms or isobars.

In simulations using classical force fields, one uses a force field to describe all atomic interactions included in the studied system.[51] The intrinsic properties of the adsorbate molecules and their interactions with each other were modeled with the united atoms TraPPE force field.[52,53] The dispersion interactions between the alkane molecules and MOF framework atoms were calculated using Lennard-Jones (L–J) potential. We found that generic DREIDING-UFF[54,55] force field cannot reproduce adsorption isobars of hexane isomers in UiO-66. Figure 5a,b shows that GCMC calculations significantly overestimates adsorption for both ideal and defected MOF, which means that they overestimate the strength of the interactions between alkane molecules and UiO-66 structure. For this reason, we undertook to refine the force field used.

The Lennard-Jones potential is based on σ_{ij} factor corresponding to the range and ε_{ij} factor corresponding to the strength of the attraction between atoms (or pseudoatoms) i and j. For the initial parameters, we used DREIDING-UFF potentials mixed with standard Lorentz-Berthelot mixing rules. These combining rules are based on an arithmetic and a geometric average for the calculation of cross σ_{ij} and ε_{ij} parameters, respectively. Fitting was performed using data and models for the defect-free material, i.e. experimental data for UiO-66_220 C and ideal UiO-66_0 structure. For each hexane isomers, we calculated three points for 453, 393, and 333 K corresponding to low, intermediate and saturation loading on the experimental adsorption isobars. The quality of the fit was determined based on the sum of the absolute values calculated for the differences between experimental A_{exp} and simulated A_{sim} adsorption [Eq. (1)] amounts for all 15 points (3 points for 5 adsorbates).

$$|\Delta A| = \sum |A_{exp} - A_{sim}| \quad (1)$$

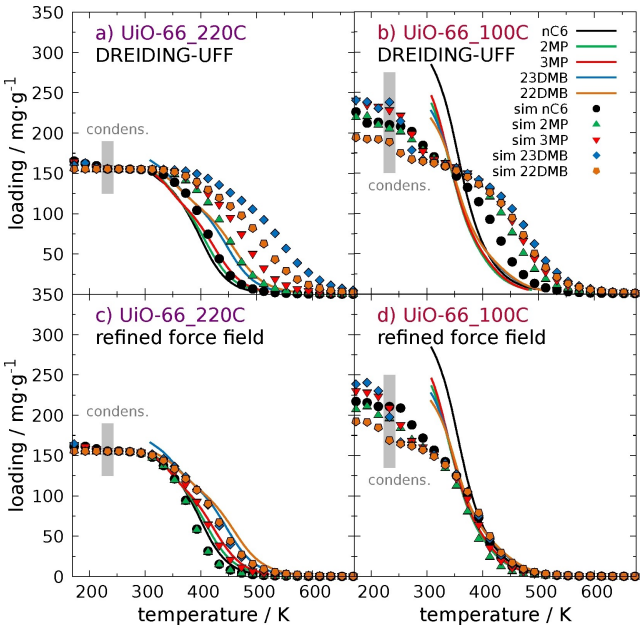

Figure 5. Adsorption isobars of hexane isomers in UiO-66. Lines stand for the experimental QE-TPDA data for the defect-free UiO-66_220 C (a,c) and the defected UiO-66_100 C (b,d). Points were simulated with GCMC for ideal UiO-66_0 (a,c) and the most defected UiO-66_32 (b,d) models of structure. Grey rectangles indicate the estimated condensation temperature of pure adsorbates taken from NIST database.[63] The partial pressures of nC6, 2MP, 3MP, 23DMB, 22DMB were relatively low ($0.02 < p/p0 < 0.04$), ca. 910, 580, 510, 710, and 970 Pa for UiO-66_220 C, while 780, 560, 520, 660, and 830 Pa for UiO-66_100 C, respectively.

We modified the L–J well depth ε_{ij} characterizing cross-interactions between each adsorbate pseudoatoms (i: CH_3, CH_2, and CH) and the framework atoms (j: Zr, O, C, and H). The tertiary C atom of the 22DMB molecule is largely shielded by the surrounding alkyl groups thus has little effect on adsorption. In this way, the force field refinement was reduced to a three-dimensional problem, where ε_{ij} for CH_3, CH_2, and CH were changed independently.

In Figure 6 we show a surface plot of $|\Delta A|$ as a function of ε_{CH3} and ε_{CH2} (relative to the initial DREIDING-UFF coefficients), for the optimal value of ε_{CH}. There is a clear minimum on the surface of factors indicating the best fitting. Numerical values of these parameters are given in Table 3. This tedious, three-dimensional refinement is also explained in detail in the Supporting Information. To validate the new parameters, we also calculated Henry constants and adsorption enthalpies for the adsorption of hexane isomers in UiO-66. The refined force field yield very good agreement with experimental data taken from Duerinck et al.,[44] which is shown in Figure S9 in the Supporting Information. It can therefore be concluded that the results of the calculations adequately reflect the macroscopic adsorption states for hexane isomers in UiO-66.

Adsorption mechanism

It has been shown that the force field refined in this work very well reflects experimental adsorption isobars (absolute values) of hexane isomers in UiO-66 (Figure 5c,d). Figure 7 shows a more detailed analysis of the adsorption of 2MP in defect-free UiO-66 (UiO-66_220 C preparation and UiO-66_0 framework model). As molecular simulations allow for a deeper insight into the adsorption mechanism, for selected points we presented average occupation profiles in zx plane. They reveal preferential situations of the guest molecules in the studied system, while the analysis of these profiles allowed for the quantification of the distribution of the molecules in different parts of the host structure. At low temperatures (< 300 K), micropores are fully occupied. Since the unit cell of UiO-66 contains 8 tetrahedral and 4 octahedral cages, both the smaller and the larger ones (Figure 1) may contain only one molecule of C6 alkanes. Therefore, the importance of lateral interactions for adsorption is small. At higher and higher temperatures, the predominance of guest molecules adsorbed in smaller tetrahedral cages points out a preference for these adsorption sites. The same is observed for the rest of hexane isomers in the defect-free UiO-66, except that for di-branched molecules distinction between adsorption in the two types of cavities occurs in a slightly wider temperature window. This means a stronger affinity of highly branched molecules for tetrahedral cages.

Figure 8 shows adsorption isobars of 2MP in the defected UiO-66 (UiO-66_100 C preparation and UiO-66_32 framework model). The low-temperature experimental adsorption (300–

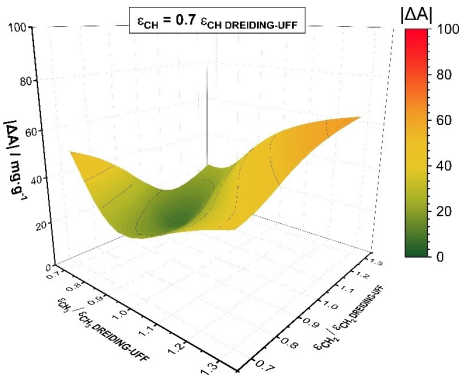

Figure 6. Surface plot of the deviation of the fit ($|\Delta A|$) as a function of ε_{CH3} and ε_{CH2} for a given $\varepsilon_{CH} = 0.7\ \varepsilon_{CH\ DREIDING\text{-}UFF}$.

Table 3. Values for the Lennard-Jones potential well depth for the initial DREIDING-UFF and the refined force fields.

force field	ε_{ij}/k_B[a]	Zr	O	C	H
DREIDING-UFF force field	CH_3	61.25	72.14	71.89	28.74
	CH_2	44.11	51.95	51.77	20.70
	CH	24.30	28.62	28.52	11.40
	C	5.27	6.21	6.19	2.47
refined force field (this work)	CH_3	49.00	57.71	57.51	22.99
	CH_2	44.11	51.95	51.77	20.70
	CH	17.01	20.03	19.96	7.98
	C	5.27	6.21	6.19	2.47

[a] the depth of L-J potential well in K.

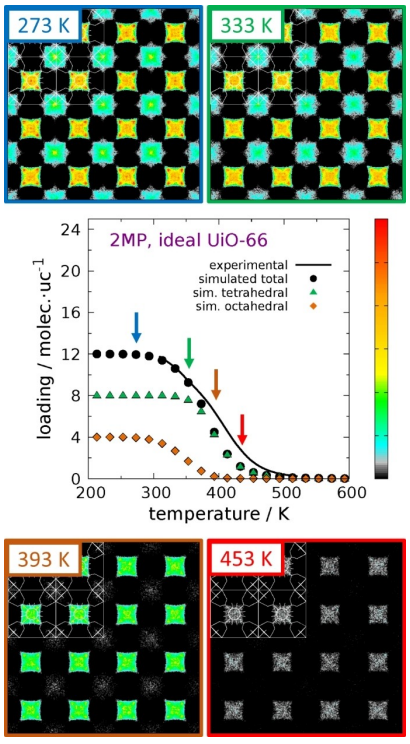

Figure 7. Experimental (line) and simulated with GCMC (black circles) adsorption isobars of 2-methylpentane in ideal UiO-66 (UiO-66_220C preparation and UiO-66_0 framework model). The calculated isobar was divided according to adsorption in different parts of the UiO-66 structure: green triangles stands for tetrahedral cavities and orange diamonds for octahedral cavities. Average occupation profiles corresponding to the four points on the calculated isobar are also shown. The partial pressure of 2MP was 580 Pa.

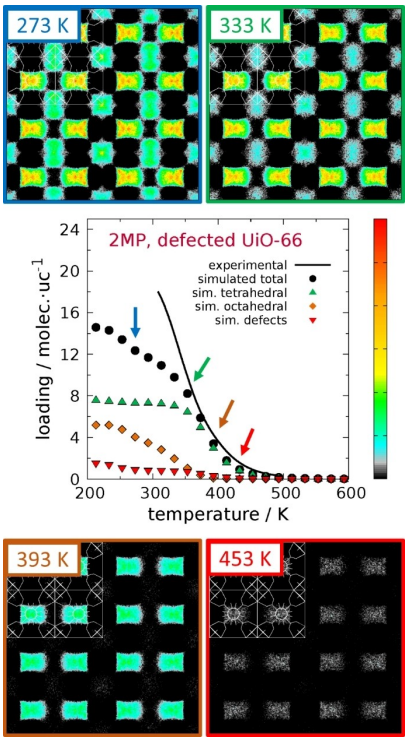

Figure 8. Experimental (line) and simulated with GCMC (black circles) adsorption isobars of 2-methylpentane in defected UiO-66 (UiO-66_100 C preparation and UiO-66_32 framework model). The calculated isobar was divided according to adsorption in different parts of the UiO-66 structure: green triangles stands for tetrahedral cavities, orange diamonds for octahedral cavities and inverted red triangles for vacancies after missing BDC linkers. Average occupation profiles corresponding to the four points on the calculated isobar are also shown. The partial pressure of 2MP was 560 Pa.

350 K) clearly exceeds GCMC calculations. This may be due to the impairment of the theoretical framework model. The exact number of defects is difficult to be accurately measured and there is a possibility that the UiO-66_100 C preparation contains more defects than its theoretical counterpart. Moreover, despite the low relative pressure of adsorptive (p/p^0 of ca. 0.02), other adsorption phenomena not related to the micropores are also possible, such as low-temperature capillary condensation between the crystallites. In fact, UiO-66_100 C has the smallest grains (ca 0.1 μm) of all preparations under this study (Figure S1 of the Supporting Information). However, the overall agreement between calculations and experimental data at higher temperatures (>350 K), where guest-host interactions are dominant, is correct. Similarly as for ideal structure, 2MP molecules tend to be located in the middle of tetrahedral cavities. As they are filled, 2MP is adsorbed in octahedral cavities and in defects located between tetrahedral cages.

A full set of the experimental adsorption isobars for the three UiO-66 preparations are presented in Figure S7 of the Supporting Information. Figure S10–S14 shows the analysis of adsorption mechanism for nC6, 3MP, 23DMB, 22DMB, including adsorption in different sites of the UiO-66 structure, similarly as it was presented for 2MP (Figure 7, 8). Generally, the contribution of defects in the adsorption process for all hexane isomers is very small, except for very high loadings (or dense packing) of the guest molecules. This may indicate that the impact of defects on adsorption is mainly manifested in a reduction in the number of non-defected tetrahedral cages.

Adsorption selectivity

The UiO-66 metal–organic framework investigated in this work is a promising candidate for use in the separation of hydrocarbon isomers.[37,38,44] QE-TPDA technique used for the experimental investigations does not allow for direct measurements for the mixtures of vapors. However, the concordance of the Monte Carlo simulations for adsorption of single component hexane isomers implies that such calculations should also give reasonable results for the multi-component mixtures. As shown in Figure 9a, the defect-free UiO-66 exhibits reverse selectivity towards alkanes as it adsorbs significantly more 23DMB and 22DMB isomers than nC6 and 2MP in a wide temperature range. Interestingly, 3MP is adsorbed in similar amounts that 23DMB, and even dominates in conditions close to saturation (T<250 K). These results confirm literature reports concerning reverse selectivity of this MOF towards branched hydrocarbons.

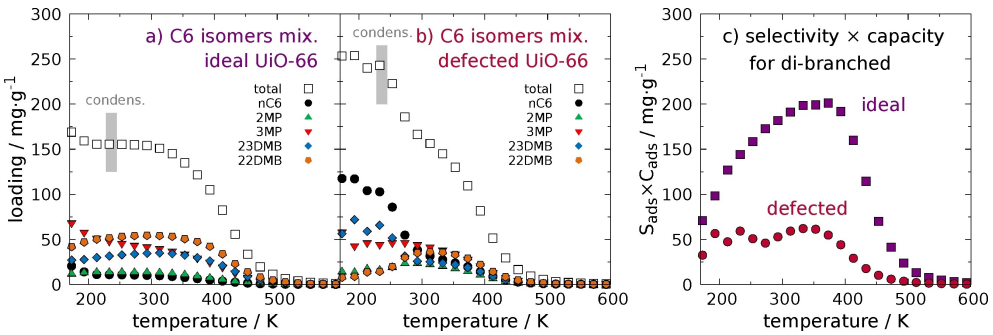

Figure 9. Simulated adsorption isobars of an equimolar mixture of hexane isomers in ideal UiO-66_0 (a) and defected UiO-66_32 (b). Grey rectangles indicate the estimated condensation temperature of pure adsorbates taken from NIST database.[63] Partial pressures of all components were equal to 1000 Pa. c) Temperature dependence of the product of adsorption selectivity S_{ads} and capacity C_{ads} with respect to di-branched hexane isomers (23DMB and 22DMB).

As shown in Figure 9b, the presence of defects in the UiO-66 structure adversely affects its selective properties towards di-branched alkanes. Although at low and intermediate loadings ($T > 350$ K) this material still rather prefers branched C6 alkanes, at high loadings ($T < 300$ K) the selectivity is reversed and resembles "normal" hierarchy where linear nC6 has the highest heat of adsorption (as for example MFI-type zeolite[41]). It seems that interconnected tetrahedral cavities no longer provide suitable voids for bulky molecules and these wider cavities are preferred by linear molecules that can adhere better to the walls.

The key metric that quantifies the efficacy of an adsorbent in mixture separation is adsorption selectivity S_{ads}. For a binary mixture the adsorption selectivity is defined in Equation (2):[64]

$$S_{ads} = \frac{q_i/q_j}{f_i/f_j} \tag{2}$$

where q are adsorption quantities in $mg \cdot g^{-1}$ and f are partial fugacities of components i and j. As UiO-66 is interesting adsorbent in terms of selectivity for di-branched isomers, Equation (2) can be defined by Equation (3):

$$S_{ads} = \frac{(q_{23DMB} + q_{22DMB})/(q_{nC6} + q_{2MP} + q_{3MP})}{(f_{23DMB} + f_{22DMB})/(f_{nC6} + f_{2MP} + f_{3MP})} \tag{3}$$

The same fugacities were assumed for all components in the calculations, so equation 3 is simplifies to $S_{ads} = 1.5 \cdot (q_{23DMB} + q_{22DMB})/(q_{nC6} + q_{2MP} + q_{3MP})$. We found that the defected UiO-66_32 is characterized by a very low selectivity (0.5–1.5), while ideal UiO-66_0 by moderate selectivity (1.5–3), and for both systems the selectivity increases with temperature (Figure S15 of the Supporting Information). High values of selectivity (> 2.8) are found for adsorption in non-defected UiO-66_0 at temperatures above 400 K, which correspond to low loadings of adsorbates. At these conditions, adsorption takes place only in tetrahedral cavities, which indicates that the unusual selectivity of UiO-66 is largely due to the presence of tetrahedral cavities in the porous structure of UiO-66. However, in practical use, adsorbent should also have a high adsorption capacity for the desired components, which was defined in Equation (4):

$$C_{ads} = q_{23DMB} + q_{22DMB} \tag{4}$$

Quantitatively, the capacity for selective adsorption of di-branched C6 alkanes was defined as the product of adsorption selectivity and capacity, $S_{ads} \times C_{ads}$. As shown in 9c, this value is naturally higher for non-defected UiO-66 and it varies with temperature. At temperatures above 450 K loading for all components is low, thus C_{ads} have to be low. On the other hand, at temperatures below 275 K S_{ads} is decreasing, so the $C_{ads} \times S_{ads}$. It also should be noticed, that the optimal conditions for separation process would also depend on the partial pressure of particular adsorptives. Therefore, it is better to associate it with the loading of the adsorbate.

It can be concluded that the investigated separation process should be conducted in the least defected UiO-66 material, at loading not exceeding 2/3 of the adsorption capacity, so that adsorption takes place mostly in tetrahedral cavities.

Conclusions

A wide range of experimental and simulation techniques was exploited to investigate the structure and porosity of the UiO-66 metal–organic framework, with particular emphasis on the presence of defects in the crystal lattice. A series of three UiO-66 preparations was synthesized solvothermally at different temperatures. FTIR and XRD experimental techniques revealed a different concentration of the missing 1,4-BDC linkers in the obtained materials. Adsorption measurements of N_2 and Ar showed type I adsorption isotherms, revealing that micropore volume and specific surface area significantly increase with the number of defects.

The quasi-equilibrated temperature-programmed desorption and adsorption (QE-TPDA) experimental technique has been used to investigate the adsorption behavior of hexane isomers in the studied UiO-66. Experimental QE-TPDA profiles revealed two adsorption states for adsorption of branched hexane isomers in ideal and slightly defected UiO-66, which correspond to adsorption in tetrahedral and octahedral cavities of this MOF. This effect was not observed for the most defected UiO-66 preparation. Uptake was almost twice as high for the defective material as for the ideal one, while adsorption was shifted towards lower temperatures.

Grand Canonical Monte Carlo (GCMC) molecular modeling was used to obtain insight into adsorption at the molecular level. To validate these simulations, the generic DREIDING-UFF force field was refined to make the GCMC calculations reflect the QE-TPDA adsorption isobars. It was also confirmed that the refined force field reflects well the Henry constants and adsorption enthalpies reported in the literature.

GCMC simulations revealed that adsorption of C6 alkanes in ideal UiO-66 takes place only in tetrahedral and octahedral cavities, each of which can contain at most one such molecule. This results in a low contribution of the guest-guest interactions to the adsorption process. The preferred tetrahedral cages provide suitable voids for bulky molecules, which is responsible for the unusual "reverse" selectivity of UiO-66. The introduction of defects to the crystal lattice causes interconnection of the tetrahedral cavities, which are preferred by linear molecules adhering better to the pore walls. This greatly reduces the selectivity of the material for the branched molecules. It can be concluded, that for the separation of di-branched C6 alkanes the UiO-66 material should be free from defects in crystal lattice. This process can be effective only in tetrahedral cavities for loadings up to 2/3 of the saturation loading.

It seems that the introduction of structural defects into UiO-66 has an opposite effect on the porosity of this materials than functionalization of this material by bulky groups (–Br, $–NO_2$ or $–NH_2$),[42–44] as it generally increases adsorption capacity but decreases selectivity towards branched molecules. Our research

shows that the defects in the crystal lattice of MOFs may not only affect the chemical nature of these materials resulting in enhanced adsorption of polar molecules or changes in thermal, electronic or catalytic properties.[24] The presence of defects primarily changes the microporosity of the porous solid that may have a major impact on the adsorption and separation process for non-polar molecules driven by dispersion interactions.

Experimental Section

Synthesis: A series of three UiO-66 preparations differing in the number of defects was synthesized in accordance with literature reports.[22] 621 mg (2.66 mmol) of $ZrCl_4$, 0.47 mL of 35% HCl (5.3 mmol) and 885 mg (5.32 mmol) of benzene-1,4-dicarboxylic acid (H_2BDC) were dissolved in 16 mL of N,N-dimethylformamide (DMF). Afterwards, the mixture was transferred to the 25 mL Teflon-lined autoclave and heated in oven at either 220, 160 or 100 °C for 24 h, yielding UiO-66_220 C, UiO-66_160 C, and UiO-66_100 C, respectively. The obtained products were filtered, washed with 30 mL of DMF with stirring at 100 °C for 90 minutes, and filtered again. Then, the solvent present in the materials was exchanged with methanol (MeOH) by adding 10 mL of 99.8% MeOH to dry preparations and stirring at 60 °C for 24 h. After that, each material was rinsed three times with MeOH, filtered again and dried for 2–3 h at 80 °C. This solvent exchange allows the samples to be activated at a lower temperature. All reagents and solvents were of analytical grade (Merck, Avantor) and were used without further purification.

Physiochemical characteristics: Powder X-Ray Diffraction (P-XRD) patterns were recorded at room temperature (295 K) on a Rigaku Miniflex 600 diffractometer with Cu–K α radiation ($\lambda = 1.5418$ Å) in a 2Θ range from 3° to 40° with a 0.05° step at a scan speed of $2.5° \cdot min^{-1}$. FTIR spectra were recorded on a Thermo Scientific Nicolet iS10 FTIR spectrometer equipped with an iD7 diamond ATR attachment. Spectra were normalized to the highest peak at ca. 1400 cm^{-1}. Scanning electron microscopy (SEM) images were obtained using Tescan Vega3 LMU instrument with a LaB6 emitter (voltage of 4 kV).

Adsorption measurements: Gas adsorption isotherms were measured using static volumetric Autosorb IQ apparatus (Quantachrome Instruments): N_2 at 77 K and Ar at 87 K by using CryoSync attachment. Micropore volume was calculated using t-plot, while specific surface area with Braunauer-Emmett-Teller (BET) methods. Pore size distribution was determined based on Ar measurement with NLDFT method by using the given model: Ar @ 87 K, zeolite/silica for cylindrical/spherical pores NLDFT adsorption model, which was provided by ASiQwin software from Quantachrome.

Vapor adsorption isobars of hexane isomers was studied with the quasi-equilibrated temperature programmed desorption and adsorption (QE-TPDA) experimental technique. Prior to the QE-TPDA measurements, a sample of 9–10 mg was put in a quartz tube and activated by heating it up in flow of pure helium (7.1 $cm^3 \cdot min^{-1}$) and then cooling down to room temperature (RT). Activation temperature for UiO-66_220 C and UiO-66_160 C was 300 °C, while for UiO-66_100 C it was 110 °C with 30 min of isotherm at 110 °C. Mass loss of the samples during activation were taken from the isothermal measurements. After activation, a small amount of the studied hydrocarbon (< 1 mol%) was added to the helium stream in a diffuser, which resulted in isothermal adsorption at RT. The concentration of hydrocarbon in flow was continuously monitored by a chromatographic thermal conductivity detector (TCD). Desorption from the studied MOFs was induced by heating the sample up to 300–350 °C, while adsorption by cooling it down back to RT. For each sample, we measured 3 desorption-adsorption cycles with a heating/cooling rate of 10 °C/min and another 3 with 5 °C/min. More details on the QE-TPDA technique and methodology can be found in the previous works.[62,65]

Acknowledgements

This work was supported by the National Science Centre, Poland, grant no. 2016/21/N/ST5/00868. A.S. obtained financial resources as part of financing the doctoral scholarship from the National Science Center, Poland, grant no. 2018/28/T/ST5/00274. T.J.H.V. acknowledges NWO-CW (Chemical Sciences) for a VICI grant. This research was supported in part by PL-Grid Infrastructure (grant id: plgsurface3). Research project is partly supported by program "Excellence initiative – research university" for the AGH University of Science and Technology. We thank M. Szufla for providing the samples and Prof. D. Matoga for sharing his laboratory.

Conflict of Interest

The authors declare no conflict of interest.

Data Availability Statement

The data that support the findings of this study are available from the corresponding author upon reasonable request.

Keywords: adsorption · hydrocarbons · metal–organic framework · linker vacancies · separation

[1] O. M. Yaghi, M. O'Keeffe, N. W. Ockwig, H. K. Chae, M. Eddaoudi, J. Kim, *Nature* **2003**, *423*, 705–714.
[2] L. J. Murray, M. Dinc, J. R. Long, *Chem. Soc. Rev.* **2009**, *38*, 1294–1314.
[3] J.-R. Li, R. J. Kuppler, H.-C. Zhou, *Chem. Soc. Rev.* **2009**, *38*, 1477–1504.
[4] H.-C. Zhou, J. R. Long, O. M. Yaghi, *Chem. Rev.* **2012**, *112*, 673–674, PMID: 22280456.
[5] Y. He, W. Zhou, R. Krishna, B. Chen, *Chem. Commun.* **2012**, *48*, 11813–11831.
[6] H. Wu, Y. S. Chua, V. Krungleviciute, M. Tyagi, P. Chen, T. Yildirim, W. Zhou, *J. Am. Chem. Soc.* **2013**, *135*, 10525–10532, PMID: 23808838.
[7] J. H. Cavka, S. Jakobsen, U. Olsbye, N. Guillou, C. Lamberti, S. Bordiga, K. P. Lillerud, *J. Am. Chem. Soc.* **2008**, *130*, 13850–13851, PMID: 18817383.
[8] Y. Bai, Y. Dou, L.-H. Xie, W. Rutledge, J.-R. Li, H.-C. Zhou, *Chem. Soc. Rev.* **2016**, *45*, 2327–2367.
[9] M. Kandiah, M. H. Nilsen, S. Usseglio, S. Jakobsen, U. Olsbye, M. Tilset, C. Larabi, E. A. Quadrelli, F. Bonino, K. P. Lillerud, *Chem. Mater.* **2010**, *22*, 6632–6640.
[10] S. J. Garibay, S. M. Cohen, *Chem. Commun.* **2010**, *46*, 7700–7702.
[11] W. Morris, C. J. Doonan, O. M. Yaghi, *Inorg. Chem.* **2011**, *50*, 6853–6855, PMID: 21711030.
[12] M. Kim, J. F. Cahill, H. Fei, K. A. Prather, S. M. Cohen, *J. Am. Chem. Soc.* **2012**, *134*, 18082–18088, PMID: 23039827.
[13] V. Guillerm, F. Ragon, M. Dan-Hardi, T. Devic, M. Vishnuvarthan, B. Campo, A. Vimont, G. Clet, Q. Yang, G. Maurin, G. Férey, A. Vittadini, S.

Gross, C. Serre, *Angew. Chem. Int. Ed.* **2012**, *51*, 9267–9271; *Angew. Chem.* **2012**, *124*, 9401–9405.
[14] G. E. Cmarik, M. Kim, S. M. Cohen, K. S. Walton, *Langmuir* **2012**, *28*, 15606–15613, PMID:23057691.
[15] X. Zhang, B. Shen, S. Zhu, H. Xu, L. Tian, *J. Hazard. Mater.* **2016**, *320*, 556–563.
[16] Z. H. Rada, H. R. Abid, J. Shang, H. Sun, Y. He, P. Webley, S. Liu, S. Wang, *Ind. Eng. Chem. Res.* **2016**, *55*, 7924–7932.
[17] Z. H. Rada, H. R. Abid, H. Sun, J. Shang, J. Li, Y. He, S. Liu, S. Wang, *Prog. Nat. Sci.* **2018**, *28*, 160–167.
[18] Z. S. Moghaddam, M. Kaykhaii, M. Khajeh, A. R. Oveisi, *Spectrochim. Acta Part A* **2018**, *194*, 76–82.
[19] S. N. Tambat, P. K. Sane, S. Suresh, O. N. Varadan, A. B. Pandit, S. M. Sontakke, *Adv. Powder Technol.* **2018**, *29*, 2626–2632.
[20] I. Abánades Lázaro, C. J. R. Wells, R. S. Forgan, *Angew. Chem. Int. Ed.* **2020**, *59*, 5211–5217; *Angew. Chem.* **2020**, *132*, 5249–5255.
[21] M. Kalaj, K. E. Prosser, S. M. Cohen, *Dalton Trans.* **2020**, *49*, 8841–8845.
[22] G. C. Shearer, S. Chavan, J. Ethiraj, J. G. Vitillo, S. Svelle, U. Olsbye, C. Lamberti, S. Bordiga, K. P. Lillerud, *Chem. Mater.* **2014**, *26*, 4068–4071.
[23] L. Liu, Z. Chen, J. Wang, D. Zhang, Z. Chen, J. Wang, Y. Zhu, S. Ling, K. Huang, Y. Belmabkhout, K. Adil, Y. Zhang, B. Slater, M. Eddaoudi, Y. Han, *Nat. Chem.* **2019**, *11*, 622–628.
[24] Y. Feng, Q. Chen, M. Jiang, J. Yao, *Ind. Eng. Chem. Res.* **2019**, *58*, 17646–17659.
[25] C. A. Trickett, K. J. Gagnon, S. Lee, F. Gándara, H. Bürgi, O. M. Yaghi, *Angew. Chem. Int. Ed.* **2015**, *54*, 11162–11167; *Angew. Chem.* **2015**, *127*, 11314–11319.
[26] G. Jajko, J. J. Gutiérrez-Sevillano, A. Sławek, M. Szufla, P. Kozyra, D. Matoga, W. Makowski, S. Calero, *Microporous Mesoporous Mater.* **2021**, 111555.
[27] P. Ghosh, Y. J. Colón, R. Q. Snurr, *Chem. Commun.* **2014**, *50*, 11329–11331.
[28] C. A. Clark, K. N. Heck, C. D. Powell, M. S. Wong, *ACS Sustainable Chem. Eng.* **2019**, *7*, 66196628.
[29] G. Jajko, P. Kozyra, J. J. Gutiérrez-Sevillano, W. Makowski, S. Calero, *Chem. Eur. J.* **2021**, *27*, 14653.
[30] W. Xiang, J. Ren, S. Chen, C. Shen, Y. Chen, M. Zhang, C. Liu, *Appl. Energy* **2020**, *277*, 115560.
[31] P. Iacomi, F. Formalik, J. Marreiros, J. Shang, J. Rogacka, A. Mohmeyer, P. Behrens, R. Ameloot, B. Kuchta, P. L. Llewellyn, *Chem. Mater.* **2019**, *31*, 8413–8423.
[32] W. Vermeiren, J. P. Gilson, *Top. Catal.* **2009**, *52*, 1131–1161.
[33] J. A. C. Silva, A. E. Rodrigues, *AIChE J.* **1997**, *43*, 2524–2534.
[34] M. Schenk, S. L. Vidal, T. J. H. Vlugt, B. Smit, R. Krishna, *Langmuir* **2001**, *17*, 1558–1570.
[35] X. Yang, M. A. Camblor, Y. Lee, H. Liu, D. H. Olson, *J. Am. Chem. Soc.* **2004**, *126*, 10403–10409, PMID: 15315456.
[36] R. A. Meyers, in *Handbook of Petroleum Refining Processes* (Eds. R. A. Meyers), McGraw-Hill, New York **2004**, Ch. 9.4.
[37] P. S. Bárcia, D. Guimarães, P. A. Mendes, J. A. Silva, V. Guillerm, H. Chevreau, C. Serre, A. E. Rodrigues, *Microporous Mesoporous Mater.* **2011**, *139*, 67–73.
[38] D. Dubbeldam, R. Krishna, S. Calero, A. Z. Yazaydin, *Angew. Chem. Int. Ed.* **2012**, *51*, 11867–11871; *Angew. Chem.* **2012**, *124*, 12037–12041.
[39] P. S. Bárcia, J. A. Silva, A. E. Rodrigues, *Microporous Mesoporous Mater.* **2005**, *79*, 145–163.
[40] A. F. P. Ferreira, M. C. Mittelmeijer-Hazeleger, A. Bliek, *Adsorption* **2007**, *13*, 105–114.
[41] A. Sławek, J. M. Vicent-Luna, B. Marszałek, W. Makowski, S. Calero, *J. Phys. Chem. C* **2017**, *121*, 19226–19238.
[42] P. A. P. Mendes, F. Ragon, A. E. Rodrigues, P. Horcajada, C. Serre, J. A. C. Silva, *Microporous Mesoporous Mater.* **2013**, *170*, 251–258.
[43] X. Dong, Q. Fan, W. Hao, Y. Chen, *Comput. Theor. Chem.* **2021**, *1197*, 113164.
[44] T. Duerinck, R. Bueno-Perez, F. Vermoortele, D. E. De Vos, S. Calero, G. V. Baron, J. F. M. Denayer, *J. Phys. Chem. C* **2013**, *117*, 12567–12578.
[45] W. Makowski, M. Mańko, P. Zabierowski, K. Mlekodaj, D. Majda, J. Szklarzewicz, W. Łasocha, *Thermochim. Acta* **2014**, *587*, 1–10.
[46] A. Sławek, J. M. Vicent-Luna, B. Marszałek, B. Gil, R. E. Morris, W. Makowski, S. Calero, *Chem. Mater.* **2018**, *30*, 5116–5127.
[47] A. Sławek, K. Roztocki, D. Majda, S. Jaskaniec, T. J. H. Vlugt, W. Makowski, *Microporous Mesoporous Mater.* **2021**, *312*, 110730.
[48] K. Roztocki, M. Lupa, A. Sławek, W. Makowski, I. Senkovska, S. Kaskel, D. Matoga, *Inorg. Chem.* **2018**, *57*, 3287–3296, PMID:29498839.
[49] K. Roztocki, M. Szufla, M. Hodorowicz, I. Senkovska, S. Kaskel, D. Matoga, *Cryst. Growth Des.* **2019**, *19*, 7160–7169.
[50] K. Roztocki, F. Formalik, A. Krawczuk, I. Senkovska, B. Kuchta, S. Kaskel, D. Matoga, *Angew. Chem. Int. Ed.* **2020**, *59*, 4491–4497; *Angew. Chem.* **2020**, *132*, 4521–4527.
[51] D. Frenkel, B. Smit, in Understanding Molecular Simulation (Second Edition), (Eds: D. Frenkel, B. Smit); Academic Press, San Diego, **2002**, p. 1–6.
[52] M. G. Martin, J. I. Siepmann, *J. Phys. Chem. B* **1998**, *102*, 2569–2577.
[53] M. G. Martin, J. I. Siepmann, *J. Phys. Chem. B* **1999**, *103*, 4508–4517.
[54] S. L. Mayo, B. D. Olafson, W. A. Goddard, *J. Phys. Chem.* **1990**, *94*, 8897–8909.
[55] A. K. Rappe, C. J. Casewit, K. S. Colwell, W. A. Goddard, W. M. Skiff, *J. Am. Chem. Soc.* **1992**, *114*, 10024–10035.
[56] D. Dubbeldam, A. Torres-Knoop, K. S. Walton, *Mol. Simul.* **2013**, *39*, 1253–1292.
[57] D. Dubbeldam, S. Calero, D. E. Ellis, R. Q. Snurr, *Mol. Simul.* **2016**, *42*, 81–101.
[58] A. Schaate, P. Roy, A. Godt, J. Lippke, F. Waltz, M. Wiebcke, P. Behrens, *Chem. Eur. J.* **2011**, *17*, 6643–6651.
[59] S. Jakobsen, D. Gianolio, D. S. Wragg, M. H. Nilsen, H. Emerich, S. Bordiga, C. Lamberti, U. Olsbye, M. Tilset, K. P. Lillerud, *Phys. Rev. B* **2012**, *86*, 125429.
[60] Y. Han, M. Liu, K. Li, Y. Zuo, Y. Wei, S. Xu, G. Zhang, C. Song, Z. Zhang, X. Guo, *CrystEngComm* **2015**, *17*, 6434–6440.
[61] A. Sławek, J. M. Vicent-Luna, B. Marszałek, S. R. G. Balestra, W. Makowski, S. Calero, *J. Phys. Chem. C* **2016**, *120*, 25338–25350.
[62] A. Sławek, J. M. Vicent-Luna, B. Marszałek, W. Makowski, S. Calero, *J. Phys. Chem. C* **2017**, *121*, 25292–25302.
[63] E. W. Lemmon, M. O. McLinden, D. G. Friend, in NIST Chemistry WebBook, NIST Standard Reference Database Number 69 (Eds: P. Linstrom, W. Mallard); National Institute of Standards and Technology, retrieved June 16, **2021**.
[64] A. L. Myers, in Chemical Thermodynamics for Industry (Eds: T. Letcher) The Royal Society of Chemistry, **2004**, p. 243–253.
[65] W. Makowski, Ł. Ogorzałek, *Thermochim. Acta* **2007**, *465*, 30–39.

Manuscript received: January 4, 2022
Accepted manuscript online: March 21, 2022
Version of record online: ■■, ■■■

RESEARCH ARTICLE

The presence of structural defects in the crystal lattice of the microporous UiO-66 metal–organic framework affects the adsorption and separation of constitutional isomers of hexane. Experimental adsorption isobars were recreated using Monte Carlo molecular modelling in order to fully understand the observed phenomena at the molecular level.

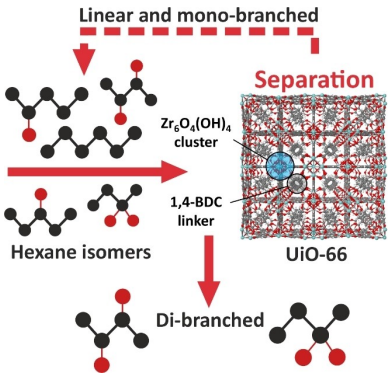

Dr. A. Sławek, G. Jajko, K. Ogorzały, Dr. D. Dubbeldam, Prof. Dr. T. J. H. Vlugt, Prof. Dr. W. Makowski*